GAMM-Mitt. **38**, No. 2, 268 – 284 (2015) / **DOI** 10.1002/gamm.201510015

Multiscale cohesive zone modeling of crack propagations in polycrystalline solids

Houfu Fan[1] and **Shaofan Li**[*1]

[1] Department of Civil and Environmental Engineering, University of California, Berkeley, CA94720

Received 23 April 2015, revised 30 May 2015, accepted 6 July 2015
Published online ? August 2015

Key words Cohesive zone model, Crack, Cauchy-Born rule, Polycrystalline solids

In this work, we use an atomistic-based multiscale cohesive zone model (MCZM)to simulate crack propagations in polycrystalline solids. The multiscale cohesive zone model is different from the conventional cohesive zone model, and it is essentially an interphase process zone that is capable of describing heterogenous material behavior by incorporating the finite-size inhomogeneities such as grain boundary interphase, inclusions, and finite-width persistent slip bands.

The main novelties of this work are two: (1) Different order Cauchy Born rules of the same atomistic potential are used to describe the material strength for the grain interphase and bulk materials, which eliminates the setback of the conventional cohesive zone model that models the undamaged material as a "numerical composite" of bulk elements and cohesive interface zones, and (2) Via integration by parts, we can derive the microstructure-based interface cohesive law in both normal and tangential directions with respect to the boundary between bulk elements and interphase elements.

By using the higher order Cauchy-Born rule, we can show that the cohesive zones are weaker than the bulk. Numerical examples of crack propagations due to the high speed impact on materials with various cohesive strengths have been carried out. Both inter-granular and trans-granular fractures are captured by assuming the relative strength of the cohesive zones in the bulk and those along the grain boundaries.

1 Introduction

Polycrystalline solids, such as metals, alloys or ceramics are extensively used in many engineering applications. In polycrystalline solids, each grain has a unique crystallographic orientation, shape, and size, which are connected by a network of the grain boundary that is usually the weakest link in polycrystalline solids. To model mechanical behaviors of polycrstalline solids , many methods have been developed at various scales, ranging from Quantum Mechanical (QM), classical Molecular Dynamics (MD), Monte Carlo simulation (MC) to Geometrical Models (GM) and Continuum Mechanics (CM) [1]. For instance, Counts et al. (2009) employed ab-initio calculations (based on QM) to design bcc Mg-Li alloys for ultra-lightweight applications [2]. By using classic MD calculations [3], Yamakov et al.(2004) investigated the transition with decreasing size from a dislocation-based to a grain-boundary based mechanism

* Corresponding author: e-mail: shaofan@berkeley.edu, Phone: +01 510 642 5362, Fax: +01 510 643 8928

of nanocrystalline metals. At the macroscale, continuum damage models, e.g. [4–7], and in particular the cohesive zone model (CZM) ([8–12]) are the two main approaches that are used to model the damage and fracture in polycrystalline solids. However, these models cannot directly include the atomistic information at nano/micro scale, and increasingly more and more people adopt the multiscale method approach to study the strength of polycrystalline solids at macro level by taking into account the information at nano/micro scale. For instance, Houtte et al. (2006) developed a hierarchical multilevel method for plastic deformation of polycrystalline materials, which consists of macroscopic models of which the parameters are to be determined through a sub level calculations [13]; and Sfantos and Aliabadi (2007) developed a multiscale boundary element method to study the material's degradation and fracture [14].

In this work, we are focusing on using the multiscale cohesive zone model (MCZM) [15] to simulate fracture in polycrystalline solids. In the MCZM, a two scale of coarse graining are considered: one for the bulk medium and the other for the material interphase, in which both the constitutive relations for both bulk materials as well as the interphase zone are constructed based on the atomistic potential, which takes into account the information of lattice microstructure, and the Cauchy-Born rule is used to describe the corresponding deformations inside. The MCZM has been employed to solve many practical problems. For instance, He and Li (2011) used a multiscale embedded atom cohesive process zone finite element model to simulate crack propagation in hyperelastic medium [16]; Zeng and Li (2012) employed the method to study fracture in composites [17]; Liu and Li (2012) proposed a finite temperature multiscale interphase zone model to study fracture process of metallic materials at finite temperature [18]. In particular, Qian and Li (2011) have used the multiscale cohesive zone model to study fracture in polycrystalline solids [19].

There are some key differences between the current work with that of [19]. In the original work of Qian and Li [19], there are two main issues: (1) In the original MCZM formulation, the deformation inside the cohesive zone is assumed to be homogeneous, and hence the first order Cauchy-Born rule is employed in the interphase zone. To model the defect, a depletion potential is employed to distinguish the bulk material and the interphase zone, which essentially replaces an undamaged material with a composite material, even though in a weak sense, the polycrystalline solid is a composite materials. However, this approach would limit for the case of intergranular fracture. If one would like to model transgranular fracture by using MCZM, one has to treat a single crystal as a composite media even before the damage occurs. (2) Different from the conventional cohesive zone model, MCZM treats the interface as a finite-thickness interphase, which introduces another geometric parameter — the thickness of the interphase. In practice, how to choose such thickness parameter is debatable. In the present work, we adopt two new approaches to deal with these two issues: (1) Employing the higher order Cauchy-Born model to model the interphase zone and replacing the previous depletion potential approach, and (2) Using integration by parts technique to convert the interphase approach to the interface approach again, which not only reduces the order of the finite element interpolation, but also eliminates the quadrature integration in the interphase zone, making the formulation less dependent on the interphase thickness.

This paper is organized as follows. The modeling of the polycrystalline microstructure is presented in Section 2. The theory of the MCZM is provided in Section 3, mainly focused on the modeling of the bulk and cohesive zone. The finite element formulation of the MCZM is presented in Section 4. In Section 5, we present the results of several numerical simulations. Finally, we conclude the work in Section 6.

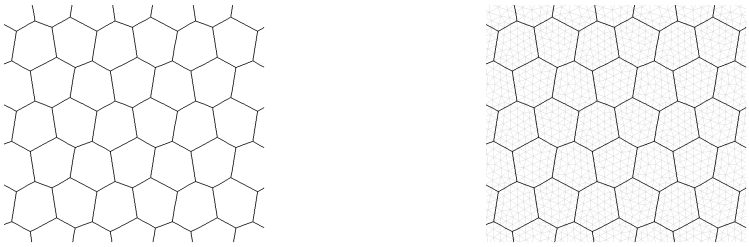

(a) (b)

Fig. 1 Polycrystal mesh generation: (a) Voronoi cell; (b)Triangular bulk elements over grains.

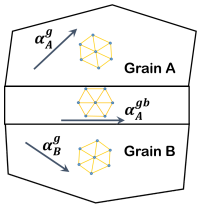

Fig. 2 (online colour at: www.gamm-mitteilungen.org) Orientation of grains and grain boundary.

2 Polycrystalline microstructure

Voronoi tessellation has been widely used to generate randomly shaped microstructure of polycrystalline solids in order to study the effect of polycrystalline grain morphology, e.g. [12, 21, 22]. It can be seen from Fig. 1(a) that each Voronoi cell represents a grain, and the edge between two neighbouring cells is considered as the grain boundary. By using the method of Delaunay triangulation, triangle bulk elements are generated inside each grain. In the cohesive Finite Element Method, cohesive zones are needed so that one can "glue" two bulk elements together. As can be seen from Fig. 1(b), the triangular meshes are conforming between adjacent grains, and it is very important in that cohesive zones are not only built up for the interphase zones in the bulk, but also those along the grain edges.

From micro perspectives, each grain has a unique lattice orientation. In this work, each grain is randomly assigned a lattice orientation α^g, which implies that all the bulk elements and the cohesive zones in one single grain will share the same lattice orientation. Note that the superscript g represents granular region and the superscript gb denotes the zones on grain boundaries. In addition, the lattice orientation of grain boundary zones α^{gb} may be assigned according to various principles or assumptions. For the sake of simplicity, in this work, the lattice orientation of a grain boundary zone is chosen to be the average of orientations from the two adjacent grains, i.e. $\alpha^{gb} = \frac{1}{2}(\alpha_A + \alpha_B)$, as shown in Fig. 2.

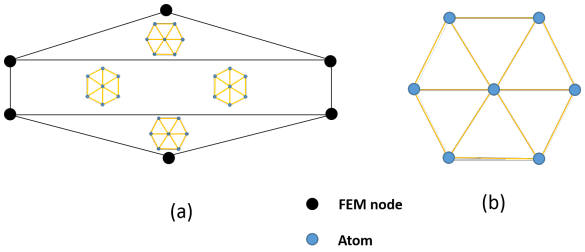

Fig. 3 (online colour at: www.gamm-mitteilungen.org) Multiscale Cohesive Zone Model: (a) Triangular bulk element and cohesive zone; (b) Hexagonal lattice.

3 The multiscale cohesive zone model

In the MCZM, a global non-uniform deformation field is discretized into a set of bulk elements with piece-wise uniform deformations, and they are connected by a finite-width cohesive zone network (elements) that have highly non-uniform deformations. By making use of lattice structure, lattice orientation and inter-atomic interaction potential, the effective constitutive properties in bulk elements can be modeled by the first order Cauchy-Born rule, as shown in Fig. 3(a). To characterize the inhomogeneous deformations in the cohesive zones, the second order Cauchy-Born rule is adopted. The deformations of cohesive elements can be obtained from the nodal displacements of surrounding bulk elements. In this way, the deformation of the bulk elements is properly connected with the nonlinear deformation field inside the cohesive zones. It is worth noting that the MCZM eliminates the discontinuous jump operator approach in description of the displacement field, which is commonly used in the conventional cohesive zone finite element method.

Without loss of generality, the following 12-6 Lennard-Jones potential is used to describe inter-atomic interactions,

$$\phi_{bulk} = 4\epsilon\left[\left(\frac{\sigma}{r}\right)^{12} - \left(\frac{\sigma}{r}\right)^{6}\right], \tag{1}$$

where ϵ the depth of the potential well, σ the finite distance at which the atomistic potential is zero, and r the atomistic bond length.

3.1 Modeling of bulk elements

In order to have an atomistic enriched constitutive model, the first order Cauchy-Born rule is adopted to develop macroscale stress-strain relation. Based on the first order Cauchy-Born rule, an arbitrary deformed bond $\mathbf{r}_i$ can be related to the original undeformed bond through as

$$\mathbf{r}_i = \mathbf{F}_e \cdot \mathbf{R}_i, \tag{2}$$

where $\mathbf{F}_e$ is the local deformation gradient tensor and can be obtained in each bulk element as

$$\mathbf{F}_e = \left.\frac{\partial \mathbf{x}}{\partial \mathbf{X}}\right|_{\mathbf{X}\in\Omega_e^b}, e = 1, 2, ..., n_{elem}^b. \tag{3}$$

As shown in Fig. 3(b), if we consider the $\{111\}$ plane of a FCC crystal, its unit cell is a six-node hexagon , then the strain energy density function in each bulk element can be expressed as

$$W_e = \frac{1}{2\Omega_0^b}\sum_{i=1}^{n_b}\phi(|\mathbf{F}_e\cdot\mathbf{R}_i|) = W_e(\mathbf{F}_e)\,, \tag{4}$$

where the superscript b indicates bulk element, Ω_0^b is the volume of the unit cell in the referential configuration; $\phi(r_i)$ is the atomistic potential, and $r_i = |\mathbf{r}_i|$ is the current bond length in a unit cell. Note that in Eq. (4) there is an $\frac{1}{2}$ factor in the front of the summation, this is because that the pairwise potential $\phi(r_i)$ is always shared by two atoms. With the strain energy density function, the constitutive relations for the bulk medium can be readily established. For instance, the first Piola-Kirchhoff stress $\mathbf{P}$ can be obtained as

$$\mathbf{P} = \frac{\partial W_e}{\partial \mathbf{F}_e} = \frac{1}{2\Omega_0^b}\sum_{i=1}^{n_b}\frac{\partial\phi}{\partial r_i}\frac{\mathbf{r}_i\otimes\mathbf{R}_i}{r_i}. \tag{5}$$

Similarly, the second Piola-Kirchhoff stress tensor and the Cauchy stress tensor can be derived as well,

$$\mathbf{S} = \frac{1}{2\Omega_0^b}\sum_{i=1}^{n_b}\frac{\partial\phi}{\partial r_i}\frac{\mathbf{R}_i\otimes\mathbf{R}_i}{r_i} \tag{6}$$

$$\boldsymbol{\sigma} = \frac{1}{2\Omega_0^b}\sum_{i=1}^{n_b}\frac{\partial\phi}{\partial r_i}\frac{\mathbf{r}_i\otimes\mathbf{r}_i}{r_i}. \tag{7}$$

3.2 Modeling of the interphase process zone

Due to the highly non-uniform deformation inside the cohesive zone, the first order Cauchy-Born rule is not suitable to be employed in deriving constitutive relation. Instead, higher order Cauchy-Born rules should be adopted. For instance, by using the second-order Cauchy-Born rule, a deformed bond vector $\mathbf{r}_i$ can be expressed as

$$\mathbf{r}_i = \mathbf{F}_c\cdot\mathbf{R}_i + \frac{1}{2}\mathbf{G}_c : (\mathbf{R}_i\otimes\mathbf{R}_i), \tag{8}$$

where the $\mathbf{G}_c$ is the derivative of the deformation gradient

$$\mathbf{G}_c = \frac{\partial\mathbf{F}_c}{\partial\mathbf{X}} = \frac{\partial^2\mathbf{x}}{\partial\mathbf{X}\otimes\partial\mathbf{X}}. \tag{9}$$

The subscript c indicates the quantity is defined within the cohesive zone. By assuming that the lattice unit cell is a hexagonal unit cell inside the cohesive zone, the corresponding strain energy density function can be written as

$$W_c = \frac{1}{2\Omega_0^c}\sum_{i=1}^{n_b}\phi\left(\left|\mathbf{F}_c\cdot\mathbf{R}_i + \frac{1}{2}\mathbf{G}_c : (\mathbf{R}_i\otimes\mathbf{R}_i)\right|\right) = W_c(\mathbf{F}_c,\mathbf{G}_c)\,. \tag{10}$$

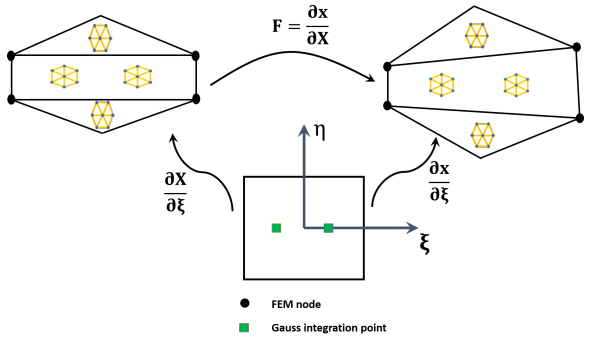

Fig. 4 (online colour at: www.gamm-mitteilungen.org) Schematic in treating the cohesive zone as a four-node quadrilateral element.

Note that W_c is a function of $\mathbf{F}_c$ and $\mathbf{G}_c$. To characterize the internal virtual work, in addition to the first Piola-Kirchhoff stress $\mathbf{P}_c$, a higher order stress couple $\mathbf{Q}_c$ is also defined in the cohesive zone. They are expressed as follows,

$$\mathbf{P}_c = \frac{\partial W_c}{\partial \mathbf{F}_c} = \frac{1}{2\Omega_0^c} \sum_{i=1}^{n_c} \frac{\partial \phi}{\partial r_i} \frac{\mathbf{r}_i \otimes \mathbf{R}_i}{r_i}, \tag{11}$$

$$\mathbf{Q}_c = \frac{\partial W_c}{\partial \mathbf{G}_c} = \frac{1}{2\Omega_0^c} \sum_{i=1}^{n_c} \frac{\partial \phi}{\partial r_i} \frac{\mathbf{r}_i \otimes \mathbf{R}_i \otimes \mathbf{R}_i}{r_i}. \tag{12}$$

As can be seen, the modeling of the cohesive zone requires the computation of both the deformation gradient $\mathbf{F}_c$ and the gradient of the deformation gradient $\mathbf{G}_c$. In two-dimensional case, if we choose the cohesive zone as a four-node quadrilateral element (see Fig. 4), it will be sandwiched by two triangle bulk elements. In terms of finite element interpolation, one can obtain

$$\mathbf{F}_c = \mathbf{I} + \frac{\partial \mathbf{N}}{\partial \mathbf{X}} \cdot \mathbf{d} \tag{13}$$

and

$$\mathbf{G}_c = \frac{\partial^2 \mathbf{N}}{\partial \mathbf{X} \otimes \partial \mathbf{X}} \cdot \mathbf{d}, \tag{14}$$

where $\mathbf{I}$ is the second-order identity matrix, $\mathbf{N}$ is FEM shape functions and $\mathbf{d}$ is the nodal displacement vector.

For a quantitative estimation on the differences of cohesive strengthes in bulk elements and cohesive zones, a benchmark test is performed on a quadrilateral element, as shown in Fig. 5 (a). The load-displacement curve is shown in Fig. 5 (b), from which one can clearly see that the peak force based on the first order Cauchy-Born rule (bulk) is higher than that of the second order Cauchy-Born rule (cohesive zone). This implies that the higher order of the non-linearity in the constitutive relations, the lower strength of the model. As a matter of fact, compared to the bulk element, the cohesive zone is a relatively weak medium, where slip lines, inclusion, dislocations and other defects might reside, and the test validates the assumption of the proposed multiscale cohesive zone model.

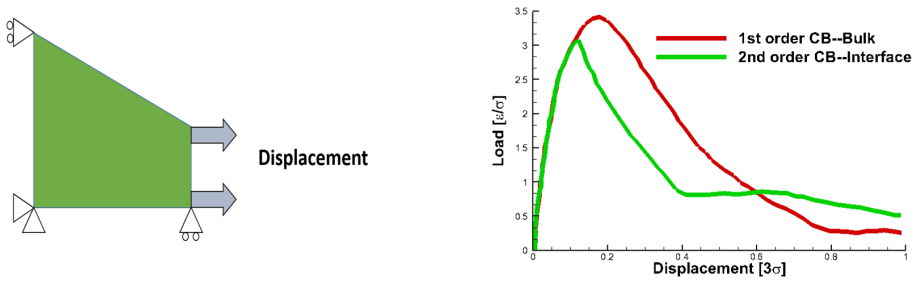

Fig. 5 (online colour at: www.gamm-mitteilungen.org) Benchmark tests for the constitutive behaviors based on the first order and the second order Cauchy-Born rules: (a) Schematic of the benchmark test; (b) Load-displacement curve.

4 Finite element formulation of MCZM

In this Section, we derive the finite element formulation for MCZM.

4.1 Galerkin weak formulation via virtual work principle

Considering a polycrystal solid Ω, we can express its total kinetic energy as,

$$\mathcal{K} = \int_{\Omega} \frac{1}{2} \rho \dot{\mathbf{u}} \cdot \dot{\mathbf{u}} dV, \tag{15}$$

where ρ is the mass density and $\dot{\mathbf{u}}$ is the velocity field in the continuum. The strain energy of the continuum can be expressed as

$$\mathcal{W}_{int} = \int_{\Omega} W(\mathbf{F}, \mathbf{G}) dV, \tag{16}$$

where $W(\cdot, \cdot)$ is the strain energy density function, which depends on both the strain measure as well as the strain gradient measure. The total Lagrangian of the system is given by

$$\mathcal{L} = \mathcal{W}_{int} + \mathcal{W}_{ext} - \mathcal{K} \tag{17}$$

where $\mathcal{W}_{ext}$ is the external potential energy. The Hamiltonian principle requires that $\mathcal{S} = \int_{t_1}^{t_2} \mathcal{L} dt$ attain its stationary value, i.e. $\delta \mathcal{S} = 0$, for all kinematically admissible variations,

$$\int_{t_1}^{t_2} \left(\delta \mathcal{W}_{int} + \delta \mathcal{W}_{ext} - \delta \mathcal{K} \right) dt = 0 \tag{18}$$

The variation of the kinetic energy is

$$\delta \mathcal{K} = \int_{\Omega} \rho \dot{\mathbf{u}} \cdot \delta \dot{\mathbf{u}} dV \tag{19}$$

Using integration by parts, one can show that

$$\int_{t_1}^{t_2} \rho\dot{\mathbf{u}} \cdot \delta\dot{\mathbf{u}} dt = \rho\dot{\mathbf{u}} \cdot \delta\mathbf{u}|_{t_1}^{t_2} - \int_{t_1}^{t_2} \rho\ddot{\mathbf{u}} \cdot \delta\mathbf{u} dt = -\int_{t_1}^{t_2} \rho\ddot{\mathbf{u}} \cdot \delta\mathbf{u} dt, \tag{20}$$

where $\delta\mathbf{u}$ is chosen to be zero at time t_1 and t_2. The first variation of the internal energy is

$$\delta\mathcal{W}_{int} = \int_\Omega \left\{ \mathbf{P}(\phi) : \delta\mathbf{F} + \mathbf{Q}(\phi) \dddot{:} \delta\mathbf{G} \right\} dV. \tag{21}$$

The first variation of the external potential energy can be expressed as

$$\delta\mathcal{W}_{ext} = -\int_\Omega \mathbf{b} \cdot \delta\mathbf{u} dV - \int_{\partial\Omega_t} \bar{\mathbf{T}} \cdot \delta\mathbf{u} dS. \tag{22}$$

The Galerkin weak form of the MCZM can be written as

$$\int_\Omega \left(\rho\ddot{\mathbf{u}} \cdot \delta\mathbf{u} + \mathbf{P}(\phi) : \delta\mathbf{F} + \mathbf{Q}(\phi) \dddot{:} \delta\mathbf{G} \right) dV = \int_\Omega \mathbf{b} \cdot \delta\mathbf{u} dV + \int_{\partial\Omega_t} \bar{\mathbf{T}} \cdot \delta\mathbf{u} dS, \tag{23}$$

which can also be expressed element-wise as,

$$\begin{aligned} &\sum_{e=1}^{n_{elem}^b} \left\{ \int_{B_0^e} \left[\rho_0 \ddot{\boldsymbol{\phi}}^h \cdot \delta\boldsymbol{\phi}^h + \boldsymbol{P}(\boldsymbol{\phi}) : \delta\boldsymbol{F}^h \right] dV \right\} \\ &+ \sum_{e=1}^{n_{elem}^c} \left\{ \int_{C_0^e} \left[\boldsymbol{P}(\boldsymbol{\phi}) : \delta\boldsymbol{F}^h + \boldsymbol{Q}(\boldsymbol{\phi}) \dddot{:} \delta\boldsymbol{G}^h \right] dV \right\} \\ &= \sum_{e=1}^{n_{elem}^b} \left\{ \int_{B_0^e} \mathbf{B} \cdot \delta\boldsymbol{\phi}^h dV \right\} + \sum_{e=1}^{n_{elem}^c} \left\{ \int_{C_0^e} \mathbf{B} \cdot \delta\boldsymbol{\phi}^h dV \right\} + \int_{\Gamma_t} \mathbf{T} \cdot \delta\boldsymbol{\phi}^h dS \,, \end{aligned} \tag{24}$$

where B_0^e represents the domain of a bulk element, C_0^e denotes the domain of a cohesive element, Γ_t is the traction boundary of the system, and $S_c^e := \partial B_0^e / \partial_t B_0^e$.

Note that all the kinematic variables with a superscript "h" represents the corresponding FEM interpolation fields. The local FEM approximation of the displacement field can be expressed as,

$$\mathbf{u}^h(\mathbf{X}) = \sum_{I=1}^{n_{node}} N_I(\mathbf{X}) \mathbf{d}_I \,. \tag{25}$$

Substituting Eq. (25) into the weak form of Eq. (24) and following the standard FEM procedure, one can obtain the discrete equations of motion as,

$$\mathbf{M}\ddot{\mathbf{d}} + \mathbf{f}^{int}(\mathbf{d}) + \mathbf{f}^{cohe}(\mathbf{d}) = \mathbf{f}^{ext} \,, \tag{26}$$

where

$$
\begin{aligned}
\mathbf{M} &= \sum_{e=1}^{n_{elem}^{b}} \int_{B_0^e} \rho_0 \mathbf{N}^{eT} \mathbf{N}^e dV, \ (a) \\
\mathbf{f}^{int} &= \sum_{e=1}^{n_{elem}} \int_{B_0^e} \mathbf{B}^{eT} \mathbf{P}^e(\mathbf{d}) dV, \ (b) \\
\mathbf{f}^{ext} &= \sum_{e=1}^{n_{elem}} \left\{ \int_{B_0^e} \mathbf{N}^{eT} \mathbf{B}^e dV + \int_{\partial_t B_0^e} \mathbf{N}^{eT} \bar{\mathbf{T}}^e dS \right\}, \ (c) \\
\mathbf{f}^{cohe} &= \sum_{e=1}^{n_{elem}^{c}} \left\{ \int_{C_0^e} \left[\mathbf{B}^{eT} \mathbf{P}_c^e(\mathbf{d}) + \mathbf{C}^{eT} \mathbf{Q}_c^e(\mathbf{d}) \right] dV \right\}, \ (d)
\end{aligned}
\tag{27}
$$

where $\sum$ is the element assemble operator, $\mathbf{N}^e$ is the element shape function matrix, $\mathbf{B}^e$ is the element strain-displacement matrix, i.e. the B-matrix, and the gradient of the stain-displacement matrix is defined as $\mathbf{C}^e := \frac{\partial^2 \mathbf{N}^e}{\partial \mathbf{X} \otimes \partial \mathbf{X}}$.

The explicit time integration is used in the computation to obtain the nodal velocities and displacements, which is based on the Newmark-beta method with $\beta = 0, \gamma = 0.5$ [23].

Note that in Eq. (27) (d), the cohesive force contribution is evaluated through a quadrature integration in the interphase, and its accuracy depends on how well the finite element interpolation field can capture the second order gradient of the displacement field. Moreover, it is also sensitive to the thickness of the interphase zone.

4.2 Interface cohesive law via integration by parts

As one may have noticed, the evaluation of the cohesive force vector $\mathbf{f}^{cohe}$ in Eq. (27) (d) requires the second derivatives of the finite element shape functions, and in this paper, the interphase zone element used is a four-node quadrilateral element, or a bilinear iso-parametric element, and it only contains one second order term polynomial xy, so it is insufficient to capture strain gradient effects.

To resolve this issue, we present an alternative approach in evaluating cohesive force contribution from the cohesive zone elements. Based on the finite element formulation presented in Eq. (27) (b) for internal cohesive force and by consecutive integration by parts, one can obtain

$$
\begin{aligned}
&\int_{\Omega_e} \Big(\mathbf{P}(\phi) : \delta\mathbf{F} + \mathbf{Q}(\phi) \vdots \delta\mathbf{G} \Big) dV \\
&= - \int_{\Omega_e} \nabla_{\mathbf{X}} \cdot (\mathbf{P} - \nabla_{\mathbf{X}} \cdot \mathbf{Q}) \cdot \delta\mathbf{u} dV + \int_{\partial\Omega_e} [(\mathbf{P} - \nabla_{\mathbf{X}} \cdot \mathbf{Q}) \cdot \mathbf{N}] \cdot \delta\mathbf{u} ds \\
&\quad + \int_{\partial\Omega_e} (\mathbf{Q} \cdot \mathbf{N}) : \delta\mathbf{F} ds,
\end{aligned}
\tag{28}
$$

in which the bulk term will disappear by considering the inertia term and body force in the interphase zone,

$$
\nabla_{\mathbf{X}} \cdot \Big(\mathbf{P} - \nabla_{\mathbf{X}} \cdot \mathbf{Q} \Big) + \mathbf{B} = \rho \ddot{\mathbf{u}} \ , \ \forall \ \mathbf{X} \in \Omega_c \ . \tag{29}
$$

Therefore, the virtual work contribution from the cohesive force becomes a boundary integration,

$$\delta W_{coh} = \int_{\partial\Omega_e} [(\mathbf{P} - \nabla_{\mathbf{X}} \cdot \mathbf{Q}) \cdot \mathbf{N}] \cdot \delta\mathbf{u} ds + \int_{\partial\Omega_e} (\mathbf{Q} \cdot \mathbf{N}) : \delta\mathbf{F} ds, \tag{30}$$

in which there are no terms that require evaluating the second derivative of FEM shape function in explicit expressions. Even though theoretically we still need them when evaluating deformed bond distance, $\mathbf{r}_i$, which implicitly depend on strain gradients. However, in actual computations, we approximate $\mathbf{r}_i \approx \mathbf{F}\mathbf{R}_i$, while using Eq. (12) to calculate the value of the couple stress. Therefore, in real computation, we never use the second derivative of FEM shape functions. It may be noted that the divergence of the first Piola-Kirchhoff stress and that of the divergence of the second order couple stress can be directly obtained analytically through Eq. (11) and (12), respectively.

In fact, if we ignore the second term in Eq. (29), Eq. (30) provides a higher order interface cohesive law,

$$\mathbf{T} := (\mathbf{P} - \nabla_{\mathbf{X}} \cdot \mathbf{Q}) \cdot \mathbf{N}, \ \forall \mathbf{X} \in \partial\Omega_e$$

which is derived from the atomistic potential inside the interphase process zone, and it reflects the lattice microstructure of the interphase zone. In principle, it should be more accurate than the empirical cohesive law used in the conventional cohesive zone model. Moreover, if we neglect the second term in Eq. (29), this atomistic-based cohesive law is also independent from the thickness of the interphase zone. Finally, we obtain a bona fide multiscale cohesive zone model without introducing any ad hoc cohesive relation and additional material parameters. The evaluation and assessment on the effects of the second term in Eq. (29) will be reported in a separated paper.

5 Numerical simulations

In this section, several numerical examples are presented, to demonstrate the capability of the proposed cohesive zone model, in the simulations of crack propagation and spall fracture in polycrystalline solids.

5.1 Crack prorogations in polycrystalline material

As shown in Fig. 6, a two-dimensional plate with dimension (2 mm $\times$ 2 mm) is subjected to unilateral tension in Y direction. Using the cohesive FEM, the plate is discretized into 121 grains and 2,376 bulk elements, which contains 3484 cohesive elements in total in the system. A pre-crack is set along several grain boundaries on the left side of the plate. The time step size is chosen to be $\Delta t = 1 \times 10^{-10} s$ in the simulation. It has been postulated that if the strength of the cohesive zone between bulk elements inside the grain is different from those on the grain boundary, the crack path might be different. In this work, the strength of the cohesive zone is characterized by the depth of the potential. Two different cases are considered in this example, i.e, $\epsilon^{gb} = \epsilon^{g}$ and $\epsilon^{gb} = 0.5\epsilon^{g}$, where ϵ^{g} denotes the depth of the potential in the cohesive zones within the grains and ϵ^{gb} represents the depth of the potential in the cohesive zones on the grain boundaries. From Fig. 7, it can be seen that a crack propagates

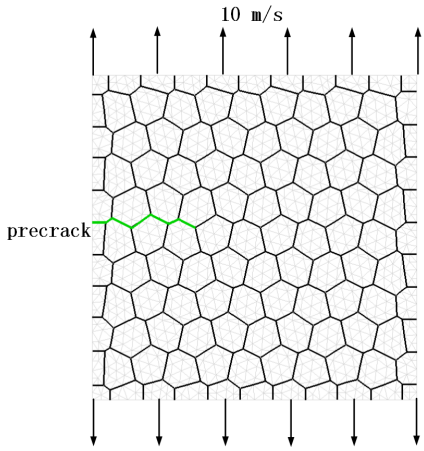

Fig. 6 Schematic of the unilateral tension

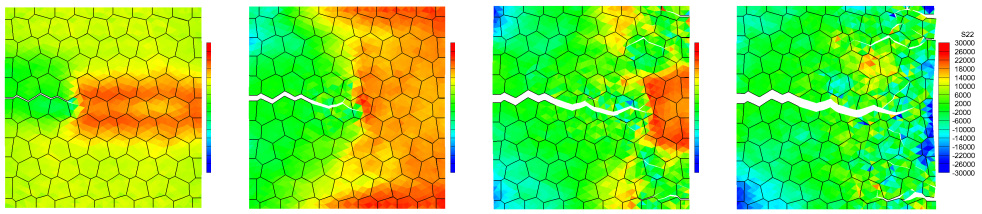

(a) (b) (c) (d)

Fig. 7 (online colour at: www.gamm-mitteilungen.org) Crack propagates through grains: (a) t=1.5 μs; (b) t=2.5 μs; (c) t=3.5 μs; (d) t=4.5μs. The simulation is conducted by adopting the second-order Cauchy-Born rule in the cohesive zone.

through grains in the first case. However, for the second case, the crack path follows closely along the grain boundaries as shown in Fig. 8.

5.2 Comparison studies

In this subsection, in order to examine numerical performance of the proposed MCZM method, a comparison simulations with exact the same parameters and problem setup of the previous transgranular fracture example has been carried out. In the comparison simulation, the deformation inside the cohesive zone is assumed to be uniform, and the first order Cauchy-Born rule is adopted in the cohesive element. The numerical result is given in Fig. 9. It can be seen that two methods produce similar crack prorogation paths. To take a closer look, the crack morphologies obtained from both methods are plotted in Fig. 10. It is shown that as the crack propagation progress, the crack surfaces become very wavy if adopting the first order Cauchy-Born rule in the cohesive zone. This can be attributed to several factors. First, the first order

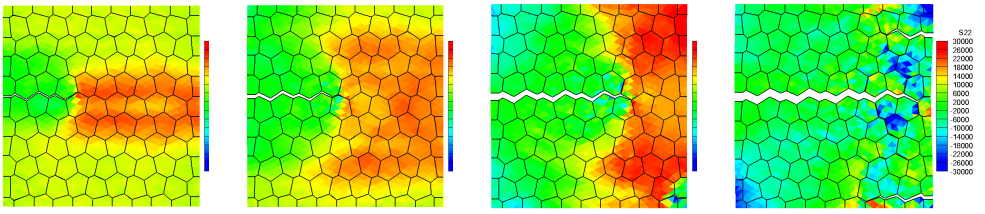

(a) (b) (c) (d)

Fig. 8 (online colour at: www.gamm-mitteilungen.org) Crack propagates along grain boundaries: (a) t=1.5 μs; (b) t=2.0 μs; (c) t=3.0 μs; (d) t=4.0μs. The simulation is conducted by adopting the second-order Cauchy-Born rule in the cohesive zone.

Cauchy-Born rule cannot correctly capture the non-uniform deformation inside the cohesive zone. Second, because of the uniform deformation assumption, zero energy modes may exist during the simulations. Consider the case with uniform deformation on a four-node cohesive zone element that is subjected to bending mode 1 or 2 (see Fig. 11 (a)). The lengths of the dotted lines and the angle between them remain unchanged during the deformation, which means that all the stress components at the integration point is zero. This cohesive element is unable to resist these type of deformations, and no stiffness is associated with any of the two bending deformations, and both are essentially zero energy modes. On the contrary, using the second order Cauchy-Born rule and adopting a reduced two-point integration in the cohesive zone element, the crack surface are very smooth. As shown in Fig. 11(b), if the cohesive element is subjected to a bending of mode 1, the horizontal dotted line clearly has a change in length, and it 'feels' the deformation, which will produce non-zero stress components in the two integration points, indicating that this type of mode can be characterized in the two-point reduced integration. Apparently, if the cohesive element is subjected to a bending of mode 2, the horizontal dotted line does not have any change in length, and it is also a zero-energy mode. In this study we stick to the reduced two-point integration scheme, instead of a 2×2 quadrature integration for the following reason. In MCZM, the aspect ratio of a typical cohesive element is very small ($a/L = 10^{-3} \sim 10^{-1}$) [19], which means the positions of the four integration points (not shown in the figure) would almost overlap under a deformation of mode 2. Of course, there are other possible zero-energy modes, but it is generally preferred to integrate with the minimum order of integration for stability to eliminate possible zero energy modes. To keep down the computation cost, the reduced two-point integration scheme is thus adopted. Based on the result shown in Fig. 10, in practical application, the second order Cauchy-Born rule is recommended for the cohesive zones.

5.3 Simulations of spall fracture under high speed impact

Numerical simulation of spall fracture is a challenge that has been elusive for many existing numerical methods e.g. [24–26]. In this example, numerical simulations have been carried out to simulate spall fractures under high-speed impact by using the proposed model. As shown in Fig. 12, the left is a rigid block with impact velocity $v = 200m/s$, the right is the target

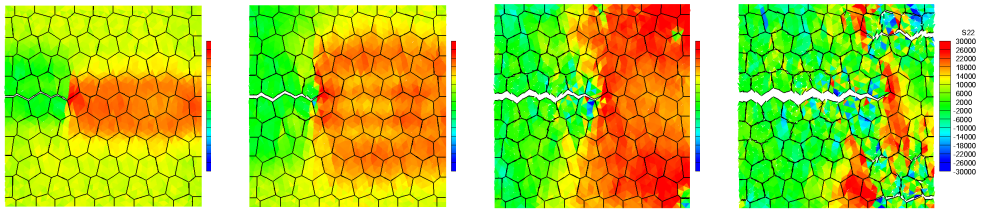

(a) (b) (c) (d)

Fig. 9 Crack propagates along grain boundaries: (a) t=1.5 μs; (b) t=2.0 μs; (c) t=3.0 μs; (d) t=4.0μs. The simulation is conducted by assuming the deformation is uniform (first order Cauchy-Born rule) in the cohesive zone.

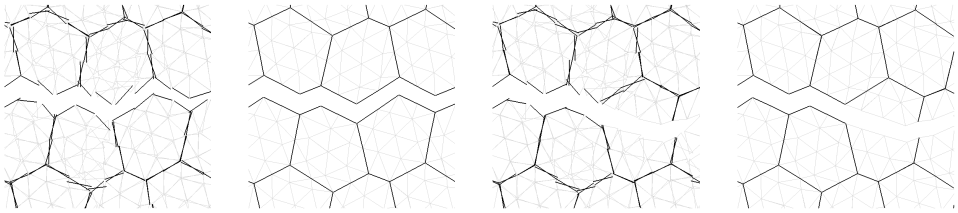

(a) (b) (c) (d)

Fig. 10 Crack surface morphologies at t = 3.0μs. (a) Trans-grainular—uniform deformation in the cohesive zone; (b) Trans-grainular—second-order Cauchy-Born rule in the cohesive zone; (c) Inter-grainular—uniform deformation in the cohesive zone; (d) Inter-grainular—second-order Cauchy-Born rule in the cohesive zone.

block with dimension 1 mm $\times$ 2 mm. The target block is discretized into 861 grains and 4,838 triangular bulk elements. The same as in the first example, the lattice orientations for bulk elements are randomly selected based on the different grains, and the orientation of the cohesive zone is set to be the average of the two adjacent bulk elements. The second order Cauchy-Born rule is adopted in the cohesive zones, and the simulation time step is chosen as $\Delta t = 1 \times 10^{-10} s$. The contact algorithm in ([27]) is employed to enforce the exact impenetrability condition in a single time step. It can be observed that the wave propagation initially starts from the contact surface, and it bounces back after reaches to the opposite boundary. By using different cohesive strengthes in cohesive elements, bulk elements, and grain boundary cohesive elements, spall fracture under high speed impacts has been successfully captured as shown in Fig. 13 and 14.

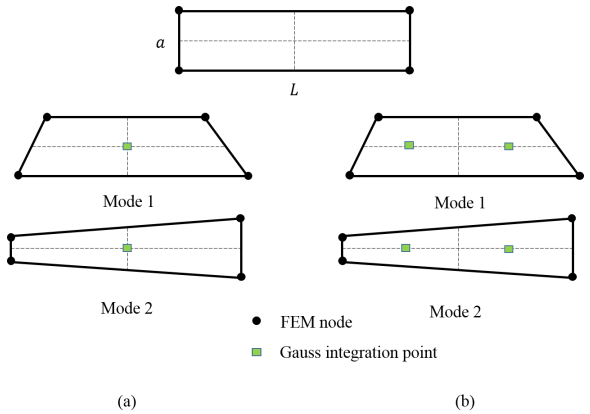

Fig. 11 (online colour at: www.gamm-mitteilungen.org) Zero energy modes of the two different approaches. (a) uniform deformation (one-point integration) in the cohesive zone; (b) non-uniform reduced two-point integration in the cohesive zone.

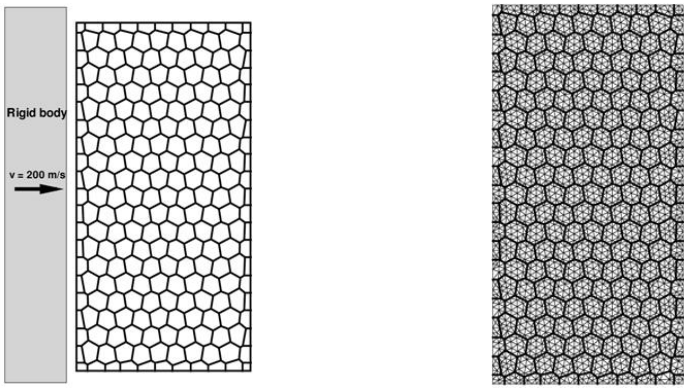

Fig. 12 Example of high speed impact: (a)Sketch of impact model; (b) Mesh of the specimen.

6 Discussions

In this work, a multiscale cohesive zone model is employed to model fractures in ploycrystalline solids. The MCZM makes use of the atomistic information, such as lattice structure and orientation in the polycrystalline solid to characterize the constitutive relations. The MCZM employs the first order Cauchy-Born rule in the bulk material and the second order Cauchy-Born rule in the cohesive zones to construct the constitutive relations of the bulk and interface based on an atomistic pair-wise potential. Using a benchmark test, it is shown that the higher order of the non-linearity in the constitutive relations, the lower strength of the model. That is, the resulting interface constitutive strength in the cohesive zones is weaker than that in the bulk, as what is expected.

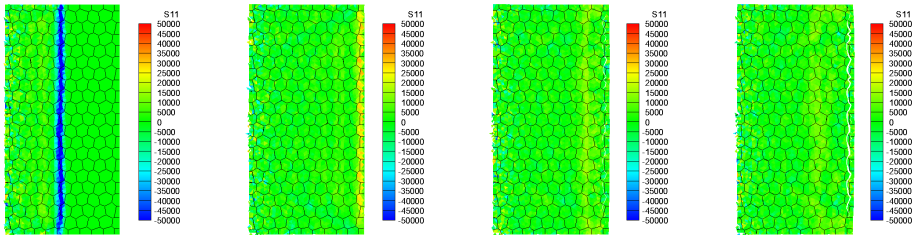

(a) (b) (c) (d)

Fig. 13 (online colour at: www.gamm-mitteilungen.org) Spall fracture propagates through grains: (a) t=0.5 μs; (b) t=1.0 μs; (c) t=1.2 μs; (d) t=1.4μs.

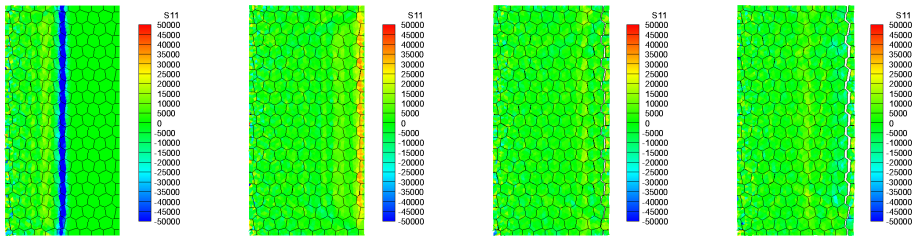

(a) (b) (c) (d)

Fig. 14 (online colour at: www.gamm-mitteilungen.org) Spall fracture propagates along grain boundaries: (a) t=0.5 μs; (b) t=1.0 μs; (c) t=1.2 μs;
(d) t=1.4μs.

It is demonstrated that the MCZM can predict both inter-granular and trans-granular fractures and their transitions in the simulation of crack propagation. Based on a comparison study of the crack surface morphologies of the simulations obtained from the first and second order Cauchy-Born rules in the cohesive zones, it is revealed that the second order Cauchy-Born and the reduced integration (2×1) in the cohesive zone are of great significance and the method proposed is much better in terms of numerical performance. The second order Cauchy-Born is better in capturing the highly non-uniform deformation in the cohesive zone and helps produce cohesive zone regions weaker than the bulk. The reduced integration is needed to eliminate the zero energy modes and avoid shear locking while at the same time, maintain the low computational cost and computation accuracy. In addition, without any artificial viscosities, the spall fracture of a specimen under high-speed impact loads are captured by using the proposed method. The numerical simulation results are in good agreements with the experimental observations.

Last, we would like to point out that the standard first order Cauchy-Born rule can only be used in macroscale constitutive modeling, when deformation is uniform. So it cannot be used in simulation of fracture or material failure, where at the crack tip the deformation is highly non-uniform and nonlinear. Moreover, the conventional cohesive zone model (CZM) uses an interface cohesive law to govern the material strength, in which the interface strength is independent from the bulk material properties. The main criticism to CZM is that it uses a "composite material" (bulk element + cohesive zone) to replace a virgin homogeneous material, because the interface is a weak zone in a priori. To overcome this difficulty, in this paper, we propose to use different order of Cauchy-Born rules for bulk elements and for interphase zones, while keeping the material's atomistic potential the same in both bulk elements and the interphase zone so that we can avoid introducing "numerical composite material" to replace the original material that is under examination.

Since higher order Cauchy-Born rule can capture nonlinear and non-uniform deformation, it makes sense to use it to simulate interphase zone, which may become a potential defect or failure zone. This is a novel idea for establishing a local material failure criterion, which is proposed by the present author in [28]. In the present paper, we use it to simulate fracture of polycrystal materials, and we have shown that it works fine. On the other hand, the standard X-FEM uses linear elastic fracture mechanics (LEFM) fracture criterion to grow crack, which is still a phenomenological material failure criterion. Can we use the higher order Cauchy-Born rule to replace LEFM fracture criterion ? or can we use it as the fracture criterion in nonlinear material media in combination with X-FEM mesh updating technique ? We would think that this is one of the future research directions.

Acknowledgements Mr. H. Fan is partially supported by the Chinese Scholarship Council. The support is gratefully acknowledged.

References

[1] A. G. Crocker, P. E. J. Flewitt, and G. E. Smith, International Materials Reviews **50**(2), 99–125 (2005).
[2] W. A. Counts, M. Friák, D. Raabe, and J. Neugebauer, Acta Materialia **57**(1), 69–76 (2009).
[3] V. Yamakov, D. Wolf, S. R. Phillpot, A. K. Mukherjee, and H. Gleiter, Nature materials **3**(January), 43–47 (2004).
[4] Z. P. Bazant, F. Asce, B. H. Oh, and A. M. Asce, Journal of engineering mechanics **111**(4), 559–582 (1985).
[5] F. L. Addessio and J. N. Johnson, Journal of Applied Physics **67**(7), 3275 (1990).
[6] D. R. Curran, L. Seaman, T. Cooper, and D. A. Shockey, Journal of Impact Engineering **13**(1), 53–83 (1993).
[7] H. D. Espinosa**32**(21), 3105–3128 (1995).
[8] X. P. Xu and A. Needleman, Journal of the Mechanics and Physics of Solids **42**, 1397–1434 (1994).
[9] M. Ortiz and A. Pandolfi, International Journal for Numerical Methods in Engineering **44**, 1267–1282 (1999).
[10] G. N. Wells and L. J. Sluys, International Journal for Numerical Methods in Engineering **50**, 2667–2682 (2001).
[11] N. Moes and T. Belytschko**69**, 813–833 (2002).
[12] H. D. Espinosa and P. D. Zavattieri, Mechanics of Materials **35**(3-6), 333–364 (2003).

[13] P. Van Houtte, A. K. Kanjarla, A. Van Bael, M. Seefeldt, and L. Delannay, European Journal of Mechanics - A/Solids **25**(4), 634–648 (2006).
[14] G. Sfantos and M. Aliabadi, Computer Methods in Applied Mechanics and Engineering **196**(7), 1310–1329 (2007).
[15] X. Zeng and S. Li, Computer Methods in Applied Mechanics and Engineering **199**(9-12), 547–556 (2010).
[16] M. He and S. Li, Computational Mechanics **49**(3), 337–355 (2011).
[17] X. Zeng and S. Li, International Journal for Multiscale Computatoinal Engineering **10**(5), 391–405 (2012).
[18] L. Liu and S. Li, Journal of Engineering Materials and Technology **134**(3), 031014 (2012).
[19] J. Qian and S. Li, Journal of Engineering Materials and Technology **133**(1), 011010 (2011).
[20] S. Li, X. Zeng, B. Ren, J. Qian, J. Zhang, and A. K. Jha, Computer Methods in Applied Mechanics and Engineering **229-232**(July), 87–109 (2012).
[21] S. Ghosh and Y. Liu, International Journal for Numerical Methods in Engineering **38**(January 1994), 1361–1398 (1995).
[22] J. E. Bolander and S. Saito, Engineering Fracture Mechanics **61**, 569–591 (1998).
[23] T. Belytschko, J. S. Ong, W. K. Liu, and J. M. Kennedy, Computer Methods in Applied Mechanics and Engineering **43**, 251–276 (1984).
[24] T. Antoun, L. Seaman, D. R. Curran, and G. I. Kanel, Spall Fracture (Shock wave and high pressure phenomena) (Springer, 2003).
[25] J. D. Clayton, International Journal of Solids and Structures **42**, 4613–4640 (2005).
[26] B. Ren and S. Li, International Journal for Numerical Methods in Engineering **93**(December 2012), 989–1014 (2013).
[27] T. J. Hughes, R. L. Taylor, J. L. Sackman, A. Curnier, and W. Kanoknukulchai , Computer Methods in Applied Mechanics and Engineering **8**, 249–276 (1976).
[28] S. Li and B. Ren, and H. Minaki [2014], Multiscale crystal defect dynamics: A dual-lattice process zone model, *Philosophical Magazine*, **94**, 1414-1450.

